Investigation of Microstructure, Mechanical Properties, and Numerical Modeling of Ti6Al4V Joints Produced by Friction Stir Spot Welding

F.A. García-Castillo, Luis A. Reyes, C. Garza, O.E. López-Botello, G.M. Hernández-Muñoz, and P. Zambrano-Robledo

In this work, lap-joined titanium alloy sheets have been successfully spot welded using friction stir spot welding (FSSW). Fully consolidated spot welds of thin Ti6Al4V sheets were obtained with a convex scrolled polycrystalline cubic boron nitride probe. The influence of processing parameters on FSSW was evaluated through a finite element analysis (FEA). Numerical results showed that von Mises stress and strain distributions were non-symmetric in the stir zone, whereas higher temperatures were observed in the region next to the tool pin. The welding microstructures showed different effects due to temperature gradients and material flow. The tool configuration played a significant role when determining the spot weld quality, since it directly influences the flow behavior of FSSW. It was observed that, in the stir zone, the microstructure suffered a transformation from α to β. The effect of welding parameters and the development of a FEA for the friction stir spot process were explored in the current investigation.

1. Introduction

Frequently, high-strength titanium (Ti) alloys are used as structural materials for the fuselage in aircrafts due to their extraordinary weight–strength ratio (Ref 1-4). Fusion welding processes are traditionally used to weld these alloys. However, conventional welding techniques applied to Ti alloys result in the formation of coarse microstructures, large deformations, and high stresses. Appropriate welding techniques for Ti alloys are essential for diverse manufacturing applications. The success of the joining process depends on the development of new welding technologies.

Friction stir welding (FSW) is a joining process that employs a permanent tool that is inserted into the abutting edges of the base metal, initially developed to joint Al alloys (Ref 5). Trimble et al. (Ref 6) state that this joining process is widely used for materials difficult to weld. Nevertheless, according to Troumpis et al. (Ref 7), basic knowledge of the friction process of high-strength materials is limited. FSW avoids problems related to solidification since bulk melting of the material does not occur during the process. Residual stresses and associated distortions are notably reduced during FSW because of the lower welding temperatures compared with those used in fusion welding (Ref 8). During the FSW process, a rotary pin produces heat via friction between the tool and the plate; the induced deformation completes the welding process (Ref 9). Fujii et al. (Ref 10) friction welded Ti at a speed ranged from 50 to 300 mm/min, reaching a temperature below the transformation of α/β phase. Mirinov et al. (Ref 11) remark that a fundamental understanding of FSW and crystallographic aspects of the transformed β microstructure in Ti6Al4V is required. Kitamura et al. (Ref 12) have described the microstructure and deformation characteristics of friction welding of Ti and Ti alloys. Lee and Lin (Ref 13) performed high-temperature deformation tests and proposed a formulation that defines and calculates the flow reaction. Liu et al. (Ref 14) evaluated joints of Ti6Al4V alloy to analyze how microstructure, mechanical properties, and welding parameters are related in the FSW of Ti6Al4V. Zhou et al. (Ref 15) analyzed the structural transformation and mechanical properties of the Ti6Al4V joints at different rotation speeds of the FSW tool, in order to establish that a full lamellar microstructure can be generated in the weld zone depending on the rotation speed, whereas the microstructure in the heat-affected zone (HAZ) was not disturbed by rotation speed. Wang et al. (Ref 16) investigated the wearing effects of different tool materials, describing the influence of a bigger pin design in deformation reduction. Yoon et al. (Ref 17) showed that the two types of morphologies are typically present in the stirring zone, and they observed a completely lamellar morphology near the top surface, while a fully equiaxed microstructure was observed near the lowest surface. Despite the previous research discussed in FSW, different aspects of the microstructural evolution of this welding technique still need to be understood in order to obtain reliable joints in different industrial sectors.

Aval (Ref 18) used friction stir spot welding (FSSW) as an alternative technique to spot weld joints. FSSW has been

F.A. García-Castillo, Universidad Autónoma de Nuevo León, Facultad de Ciencias Físico Matemáticas, Pedro de Alba, Ciudad Universitaria, 66451 San Nicolás de los Garza, N.L., Mexico; **Luis A. Reyes, C. Garza, G.M. Hernández-Muñoz,** and **P. Zambrano-Robledo**, Universidad Autónoma de Nuevo León, Facultad de Ingeniería Mecánica y Eléctrica, Centro de Investigación e Innovación en Ingeniería Aeronáutica, Carr. a Salinas Victoria km. 2.3 Aeropuerto Internacional del Norte, C.P. 66600 Apodaca, N.L., Mexico; **O.E. López-Botello**, Tecnológico de Monterrey, Escuela de Ingeniería y Ciencias, Ave. Eugenio Garza Sada 2501, 64849 Monterrey, Nuevo León, Mexico. Contact e-mail: luis.reyessr@uanl.edu.mx.

considered as a replacement for single-spot welding processes such as resistance spot welding and riveting. Applications of FSSW are found in high-value markets such as the aerospace, aviation, and automobile industries (Ref 19). According to Song et al. (Ref 20), the most significant parameters that affect the mechanical properties of FSSW are the rotatory speed, plunge velocity, plunge depth, and dwell time. Bozkurt et al. (Ref 21) described the FSSW process as rotating the tool at a defined velocity and plunging it into the plates; after the shoulder interacts at the top surface of the base metal, joining occurs by diffusing the materials, which is essentially caused by the pressure and temperature through the interface at microscopic level. When a predefined penetration is reached, the process resides for a time and the tool thereafter withdraws from the sample. A schematic of the FSSW process is illustrated in Fig. 1.

Typically, FSSW joints exhibit four zones: agitation or stir zone (SZ), thermomechanical-affected zone (TMAZ), heat-affected zone (HAZ), and the unaffected base metal (BM). In the SZ, the material changes substantially by elevated temperatures and deformations present during the process. On the other hand, in the TMAZ, grains are oriented parallel to the boundaries showing a marked effect of friction and temperature. Moreover, the HAZ presents a comparable microstructure to that of the BM, comprising α grains in a β matrix (Ref 22). Thermal gradients produced during the process are of great interest for researchers, since predictions of the β-transus would be of great insight of the mechanical behavior present during the process.

The finite element method (FEM) has been implemented to predict the mechanic and thermal effects of FSSW joints. This type of numerical methods attempts to develop an improved understanding of the physical phenomena occurring during the FSSW. Kim et al. (Ref 23) developed a FEM and a finite volume (FV) technique to model the thermomechanical process of FSSW for AA5083-H-18 and AA6022-T4 alloys, based on Lagrangian and Eulerian formulations, focusing in the influence of tool characteristics on weld and material flow. Fanelli et al. (Ref 24) described a physic and numerical analysis of FSSW joints by a complex 3D FEM model to estimate the mechanical characteristics of the weld; their experimental data described

the internal structure of the joint after the welding process. Mandal et al. (Ref 25) conducted a numerical study for the plunge phase in FSW by selecting a non-rigid plate model with brick elements and a rigid welding tool. Awang et al. (Ref 26) performed thermomechanical modeling of the FSSW process using an explicit adaptive meshing scheme to preserve element quality under elevated strain. D'Urso and Giardini (Ref 27) reported a numeric model of FSSW for joining thin plates using a simplified 2D model developed with the software DE-FORM®. Zhang and Zhang (Ref 28) conducted a FEM study using ABAQUS® to determine the heat transfer and mechanic flow in an FSW elastoplastic model. It has been noted that limited research of both experimental and modeled FSSW of Ti alloys is available. The understanding of the FSSW process claims to be a challenging task, since it involves multi-physical phenomena, non-stable states, and a continually deforming process and high thermal gradients. Prediction of the involved physical phenomena of the FSSW process from fundamental formulations can require numerous iterative steps in the model.

In this research, Ti6Al4V alloy sheets were spot welded using FSSW with different rotary speeds and axial feed rates, a 3-s reside time, and a total advance of 2.5 mm. Numerical models were undertaken using DEFORM® 3D in order to obtain the thermal and mechanical behavior during the FSSW of Ti6Al4V plates. The aim of this research is to understand FSSW of Ti6Al4V alloy and the impact of process variables such as rotation speed, axial speed, and reside time in the reliability of the joint.

2. Methodology

The welded plates were composed of Ti6Al4V alloy. The principal elements in weight percent are 0.019 C, 0.19 O, 0.016 N, 0.25 Fe, 6.2 Al, 3.87 V, and Ti in balance. The experiment consisted of lap joining by FSSW Ti6Al4V sheets of 50 mm × 50 mm, a height of 1.5 mm, and an intersection of 2.5 mm. The principal variables considered in the experiments were the rotation velocity, axial feed rate, and the plunging depth.
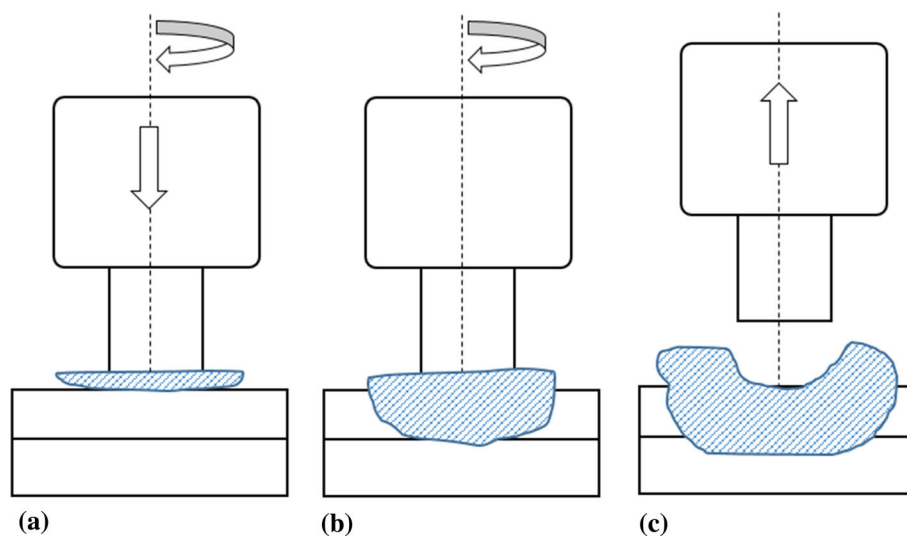

Fig. 1 Schematic of the FSSW process: (a) plunging, (b) stirring, and (c) retraction

Experiments were undertaken following a selected surface-response central composite design to estimate the principal parameters of FSSW. Random tests were considered and replicated. Table 1 shows the parameters evaluated in the central composite design. The welding parameters were lower and higher rotating velocity of 438 and 863 rpm, respectively, axial feed rates from 48 to 132 mm/min, and a total penetration of 2.5 mm. As previously reported by Garcia-Castillo et al. (Ref 22), a rotating velocity of 500 rpm induced adequate stirring of the material resulting in sound joints.

Spot welds using FSSW of the Ti sheets were performed at a Bridgeport model VMC 760 XP[3] high-speed machining center. A personalized clamping device for positioning samples was fabricated. The principal characteristics of the CNC equipment used for the welding operations are: maximum velocity of 12,000 rpm, power of 18.5 kW, and working surface of 2850×3000 mm^2. Spot welds were performed using a curved thread shoulder tool made of polycrystalline cubic boron nitride (PCBN). The tool was elongated from 36.7 mm at the shoulder to 5.9 mm at the tool end, as shown in Fig. 2. A tapered tool is necessary because of the limited thermal conductivity of Ti. Buffa et al. (Ref 29) reported that the typical design with a large shoulder and a slender pin was not adequate, since the heat produced at the shoulder cannot flow to the root of the joint to stir the Ti.

The temperature was measured by strategically located thermocouples during the friction process. The approximate location of thermocouples and the nodes selected in the numerical model correspond to analogous locations of the spot welds. The data collected were used to evaluate the process temperature. The characteristics of the final microstructure were analyzed in a Jeol 6510-LV scanning electron microscope; meanwhile, measurements of hardness were recorded in the crosswise joint section using an Instron 402MVD micro-indentation tester. Shear tests were performed to evaluate the rupture strength of the alloy. The tests were performed on a MTS Landmark model 64,725 hydraulic servo machine with a constant velocity of 1 mm/min on the welded samples.

Table 1 Parameters in the experimental design of FSSW of Ti6Al4V sheets

Test number	Rotational speed, rpm	Feed rate, mm/min
1	650	90
2	650	48
3	800	120
4	650	90
5	500	120
6	438	90
7	650	90
8	650	90
9	650	90
10	650	132
11	800	60
12	500	60
13	863	90

3. Finite Element Modeling

A 3D FEM model of the FSSW process was developed using the software DEFORM® 3D. A Lagrangian implicit program and an automatic re-meshing approach were selected to model the friction process. A fully coupled model that enables interdependent calculus of displacement and temperature in each node was defined. Sheet plates were modeled as a viscoplastic material, whereas the tool and the fixing system were modeled as non-deformable objects. Thermal properties of the PCBN tool were implemented in the numerical model, according to Swab et al. (Ref 30). Heat exchange of the bodies with the environment was considered; the support was bigger than the bulk of the sheets. Thermal properties of Ti6Al4V alloy were modeled using the DEFORM® 3D database. The contact between the tool and the plates was considered by definition of a friction model according to previous work performed by Buffa et al. (Ref 29). The selected parameters in the numerical model are enlisted in Table 2.

The Johnson–Cook constitutive model shown in Eq 1 was implemented to determine the material behavior at high deformation and elevated temperature, see Table 3. Empirical constant values were obtained from the work developed by Lee and Lin (Ref 13):

$$\sigma = \left[A + B\left(\bar{\varepsilon}^{pl}\right)^n \right] \left[1 + C \ln\left(\frac{\dot{\bar{\varepsilon}}^{pl}}{\dot{\bar{\varepsilon}}_0^{pl}}\right) \right] \left[\frac{T - T_e}{T_m - T_e} \right] \qquad \text{(Eq 1)}$$

The temperature distribution of the joint was evaluated and compared with experiments in order to validate the model results and to determine the influence of the parameters during FSSW of Ti6Al4V. For the numerical model, a blended plate was assumed instead of two separate plates to avoid numerical instabilities. However, this approach does not enable the estimation of the bonding characteristics in the welding region. Figure 3 shows the structured mesh defined during modeling. Finer mesh elements were used just below the tool shoulder defined by the mesh density option. The general mesh comprises tetrahedral elements with elements of 0.99 mm, whereas the finer mesh window presents an element of 0.4 mm. The overall mesh was defined with 85,000 elements in both weld plates.

4. Results and Discussion

Experiments were performed, and different geometries of spot welds were obtained. Figure 4 shows different spot welds made in plates of Ti6Al4V. The samples were welded according to the design of experiments described in Sect. 2.

A microstructural analysis of the Ti6Al4V base metal was carried out before the FSSW process as reference data. Figure 5(a) shows EDS results and a SEM image of the SZ of the sample welded at 500 rpm. Base metal and weld phase evolution was carried out by x-ray diffraction (XRD) as shown in Fig. 5(b) where α-Ti and β-Ti were identified in the XRD patterns of both conditions.

The microstructure after welding can be classified into four regions: SZ, TMAZ, HAZ, and BM, as previously discussed. Figure 6 illustrates the zones generated by the FSSW process, and the sample shown corresponds to the condition at 500 rpm
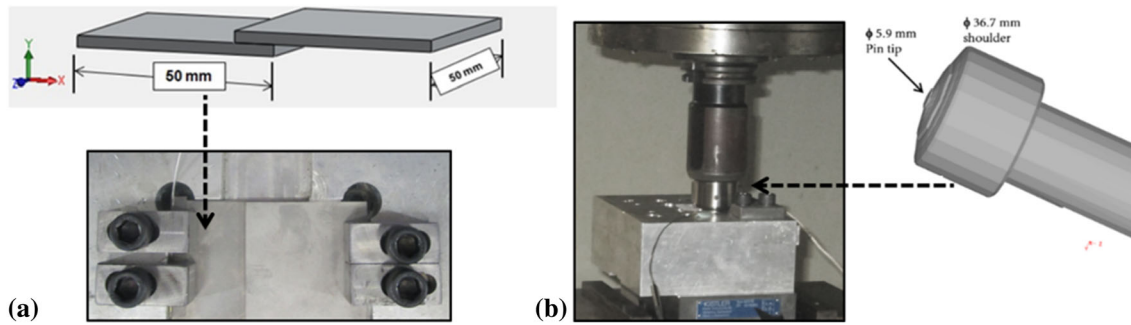
Fig. 2 Schematics: (a) welded sheets and fixing support; (b) tooling configuration and dimensions

Table 2 Considerations implemented in the numerical model of the FSSW process

FSSW model	Type/value
Model	Tridimensional
Approximation method	Lagrangian
Simulation steps	1219
Displacement per step	0.003125
Solution method	Conjugate gradient
Iteration method	Direct
Maximum number of Iterations	200
Elements	338,941
Nodes	71,121
Error convergence limit	0.005

Table 3 Johnson–Cook parameters considered for material flow during FSSW process

Constant	Symbol	Units	Value
Elastic limit (20 °C)	A	MPa	782.7
Hardening modulus	B	MPa	498.4
Deformation sensibility	n	…	0.28
Coefficient of deformation sensibility	C	…	0.028
Environment temperature	Te	°C	20
Melting temperature	Tm	°C	1662
Thermal softening coefficient	m	…	1
Plastic deformation	$\bar{\varepsilon}^{pl}$	…	1
Normalized plastic strain rate	$\dot{\bar{\varepsilon}}^{pl}$	…	1

and 120 mm/min. The intense plastic deformation at elevated temperatures produces a fine equiaxed microstructure that strengthens the material because of grain refinement. It was shown by Pilchak and Williams (Ref 31) that the welding speed strongly affects the grain size of welded Ti6Al4V. The cross-sectional microstructure of FSSW joint and estimated limits of different regions are indicated by dotted lines. Refinement is perceived in the SZ region as a consequence of the substantial deformation during friction. Typically, the SZ presents fine equiaxed grains because of the recrystallization phenomena generated during the process (Ref 19).

In Fig. 7, the transition zones are shown in detail, evidence that it can be successfully joined using the FSSW process, using a specially designed and manufactured tool of polycrystalline cubic boron nitride (PCBN). The limits between the regions are designated by the dotted lines. Refinement is

observed in the SZ region produced by the plastic effect in the same direction of the applied friction. In the TMAZ, grains are stretched in a similar direction to the boundary, indicating the evidence of plastic flow because of high contact and thermal effects during the FSSW process. Micrographs are presented for the three zones developed by the welding process. Figure 7(a) and (d) confirms the experimental results from the joints was observed a laminar morphology α + β in the SZ and a bimodal microstructure in the HAZ.

The material flow plays a fundamental role in the friction stir welding process since it determines the effectiveness of the joint. The material flow around the tool is very complex. The results depend on the correct selection of the tool geometry and the operating parameters considering the properties of the material to be joined. Hence, it is important to understand the characteristics of the material to select the optimal design of the tool and the combination of the process parameters.

The experimental design allows to determine both the most influential variables in the system as well as their correlation. In this study, the response surface methodology was used, allowing to observe the associated effects of all the factors. A composite central surface design was developed with the aim of determining optimal welding values in the Ti-6Al-4V alloy. The levels for the respective factors are lower and higher level of rotational velocity (500-800 rpm) and lower and higher level of penetration velocity (60-120 mm/min).

The formation of the bimodal microstructures in transition zones is due to the effect of the combination of phase transformation and recrystallization process. This zone exhibits hardness less than the BM, while the SZ is the part of the weld with a hardness close to the average of the BM. The decrease in hardness in the HAZ can be explained by the annealing effect caused by the heating generated by friction. Microstructures of welded joints acquired by SEM are shown in Fig. 8. An appreciable refinement in the welding button can be observed, while in the TMAZ there is grain flow and elongation. As mentioned before, the microstructure of the base plates presents a laminar α/β microstructure. The HAZ shows two different microstructures consisting of grains of α encompassed in a matrix of lamellas of α/β. The maximum temperature in the HAZ is expected to be inferior to the transus temperature corresponding to the observation of the α/β relationship performed by Muci-Küchler et al. (Ref 32). In a work developed by Xu et al. (Ref 33), it was defined that when applying a rotary velocity of 200-150 rpm, maximum welding temperatures are below β-transus temperature. However, microstructure analyses have revealed that the highest temperature during FSW regularly surpasses the β-transus, and the
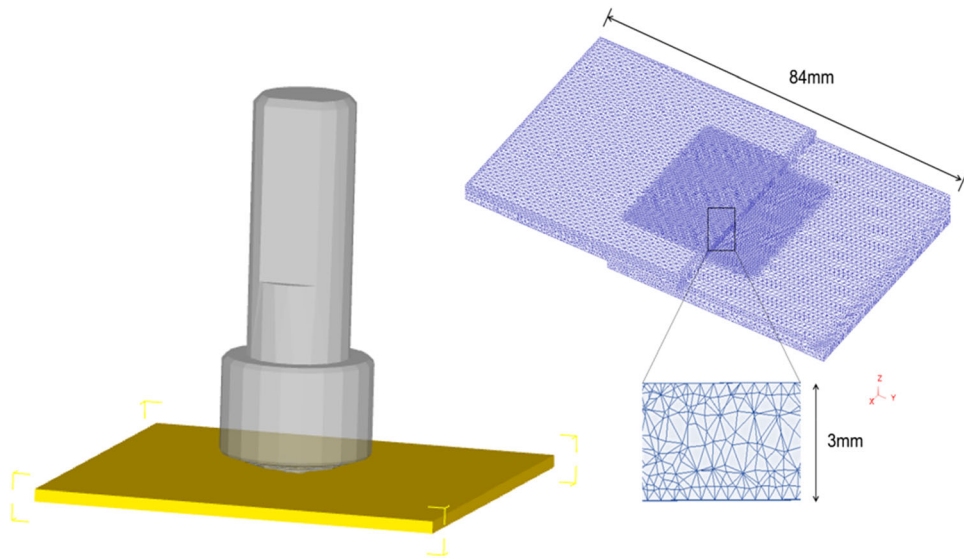
Fig. 3 Modeling and mesh characteristics of lap joining FSSW process
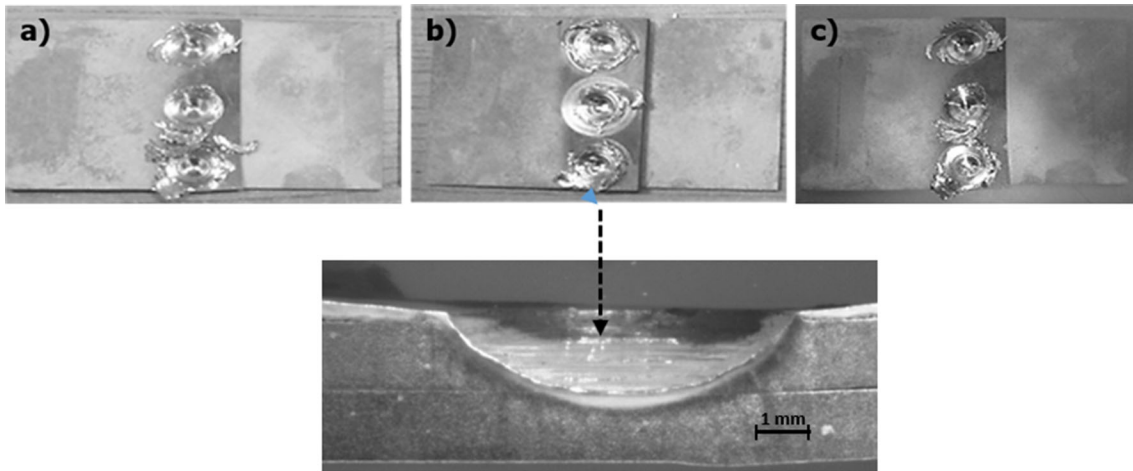

Fig. 4 Joints welded by the FSSW process: (a) 500 rpm to 60 mm/min; (b) 650 rpm to 90 mm/min and cross-sectional profile of the joint; and (c) 863 rpm to 90 mm/min
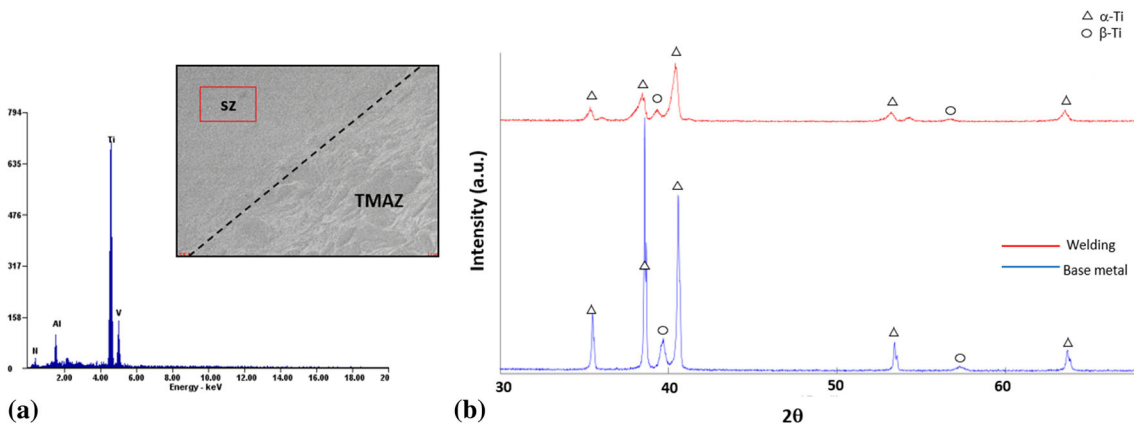

Fig. 5 (a) EDS results and SEM image of the SZ of the sample welded at 500 rpm and (b) x-ray diffraction patterns of Ti-6Al-4V of the base metal and welding

final structure is generated through β to α phase conversion during FSW cooling stage (Ref 34). According to Elmer et al. (Ref 35) in the SZ, transformation in the direction of cooling has shown to initiate under the martensite start temperature and entirely converts the microstructure to α martensite.

In the HAZ, Ti6Al4V does not experience a visible plastic deformation during the FSSW process. Consequently, any structural development in this section results from the increase in temperature. The TMAZ microstructure is located between the HAZ and SZ, being defined by the elongated grains, which

Fig. 6 Ti-6Al-4V welded cross section at 500 rpm and 120 mm/min

is indicative of deformation during spot welding by friction stirring; permanent flow occurs in the α phase, mainly by sliding dislocations. These dislocations are produced from α to β boundaries and slip in basal planes, in contrast with prismatic planes (Ref 36). The structure in the SZ is considerably affected by the speed of rotation; the refinement of grains in this zone suggests that the maximum temperature surpasses the transus temperature, forming a fully laminar microstructure (Ref 11).

Dual microstructures are generated by a combination of the phase transformation and the dynamic recrystallization. The HAZ exhibits inferior hardness values compared to those of the BM, while the SZ presents a hardness value near to the BM. The reduction in hardness in the HAZ is generated by the annealing process during the friction (Ref 14). The microstructure in the SZ is significantly influenced by the speeds of rotation and penetration. To achieve the union in the α + β titanium alloy, the temperature in the SZ must exceed the β-transus temperature, and therefore, a complete laminar microstructure is formed.

The numeric model reproduces the temperature profile and stress–strain distribution of the weld zone. Because FSSW is a
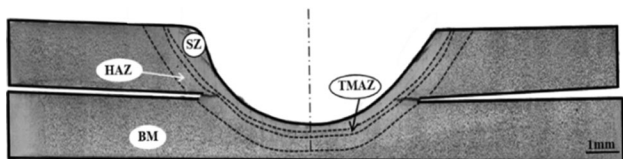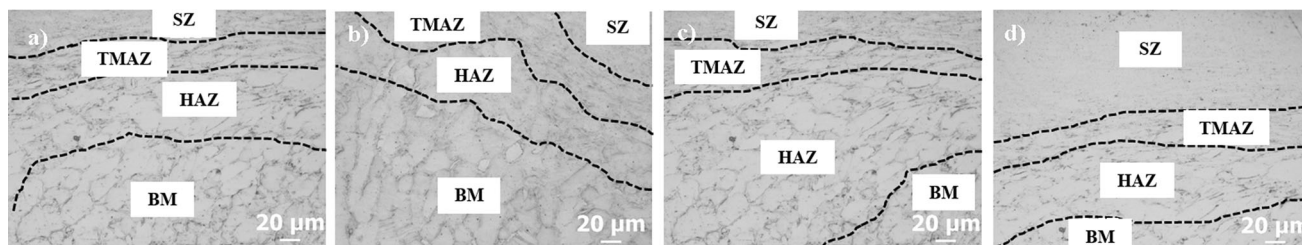

Fig. 7 Micrographs of welded joints indicating friction welding areas: (a) 650 rpm and 90 mm/min; (b) 650 rpm and 48 mm/min; (c) 800 rpm and 120 mm/min; (d) 650 rpm and 90 mm/min
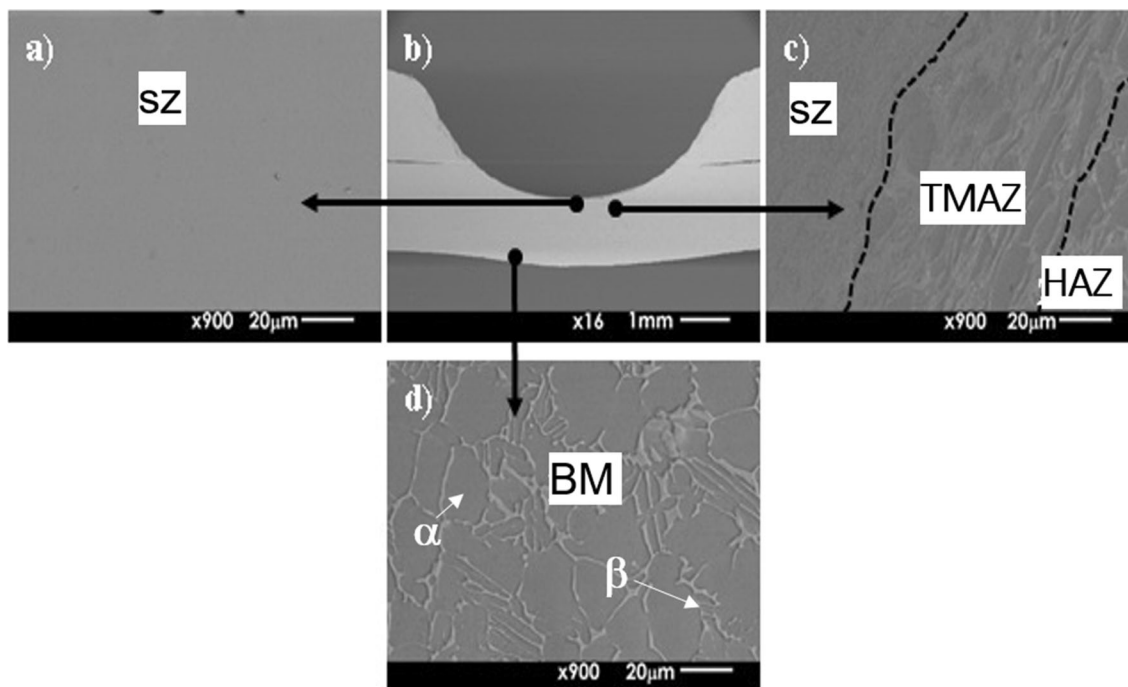

Fig. 8 Microstructure in welds of Ti6Al4V alloy by FSSW: (a) scanning electron micrograph of the SZ welded at 800 rpm and 60 mm/min; (b) the friction region; (c) the transition of the SZ, TMAZ, and HAZ; and (d) a magnified image showing the microstructure of the BM
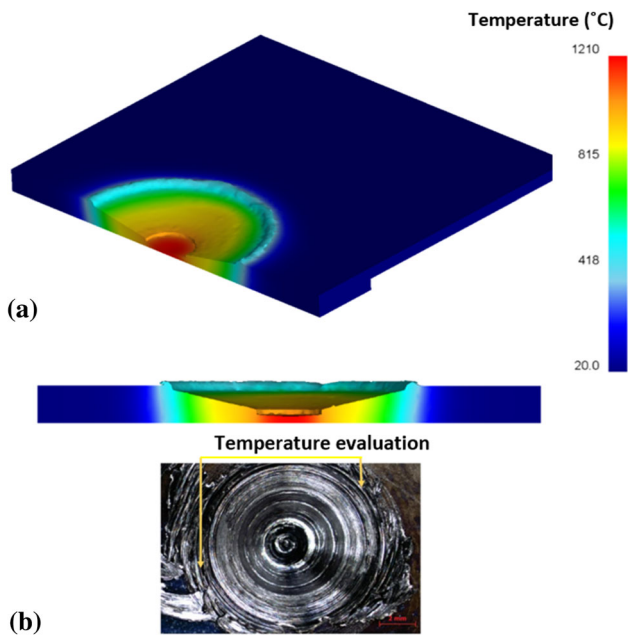
Fig. 9 (a) Three-dimensional model of the welding point and (b) welding spot generated by the FSSW process

non-melting process, the observed maximum temperatures are below the melting point of the Ti6Al4V. During the processing, the time for the plunge operation was approximately 1.2 s. From the model, a well-defined pattern of the joint caused by the convex scrolled shoulder tool was observed, see Fig. 9. FSSW creates frictional heat by rubbing the bounded interfaces of the materials while under compressive axial loads. Once the metal is plasticized and softened by the heat. The tool design substantially affected the process, in which most of the generated heat was located at the shoulder and pin configuration. The flow pattern of the convex scrolled shoulder tool promotes material transport and increases heat generation during welding. The morphology of the tool strongly influences the joint strength, which changes with the variation of the concavity angle (Ref 29). To improve the process and fabricate new FSSW tools, understanding the physics of this complex process by numerical modeling is important (Ref 33).

The numerical model predicts a non-symmetric FSSW process. The highest temperature was located near the weld center, whereas the lowest value (~ 660 °C) was observed at the nugget zone boundary. This measured region is lower than the β-transus temperature of ~ 980 °C for Ti6Al4V (Ref 31). At 600 °C, the α phase starts transforming into β phase and the transformation finishes at ~ 980 °C. Figure 10 shows how heat flows into the base metal, decreasing the maximum temperature below the tool shoulder, whereas at the center of the pin heat accumulates.

The experimental temperatures recorded at 500 rpm and 120 mm/min are shown in Fig. 10. A large temperature gradient was formed in the weld due to the low thermal conductivity of Ti6Al4V. Figure 10 also shows that the temperature gradually increases after 0.6 s of operation, reaching a peak value after 1.2 s. The temperature at a selected point of the numerical model (S1) is compared with experimental temperatures measured at three points (E1, E2, and E3) during the friction process. Experimental point E1 presents a maximum temperature of 980 °C after 1.2 s, whereas experi-

mental points E2 and E3 reached temperatures greater than 1000 °C after 1.2 s of operation. The numerical value S1 has the same trend during welding evolution with an up-and-down behavior of temperature recorded through the welding due to the thermal behavior of Ti6Al4V.

The experimental temperature for all joint conditions was recorded, see Fig. 11. Thermal history indicates a highest temperature of 1278.71 °C recorded at 800 rpm and 120 mm/min and a lowest temperature of 638.5 °C for 438 rpm and 90 mm/min. In more detail, Fig. 11(a) illustrates the temperature in welded joints at 438 rpm and 90 mm/min, 500 rpm to 60 mm/min, and 500 rpm to 120 mm/min. It was identified that the parameters that affect the properties of the welding zones were the maximum temperature and the cooling speed, highlighting that the grain size was affected mainly by the temperature. The rotation speed and the feed rate of welding were the main independent variables that had an effect on the temperature reached during the FSSW process and are those used to control it. Liu et al. (Ref 14) remarked that high transverse speeds tend to reduce the heat input and thermal gradients. Figure 11(a) shows how increasing feed-rate speed decreases the maximum temperature reached during the friction process of Ti6Al4V, contrary to the effect of the welding speed in the FSW process in aluminum alloys (AA), which can be attributed to the low thermal conductivity of Ti.

Figure 11(b) shows the temperature distribution in welded joints with 650 rpm to 132 mm/min, 650 rpm to 90 mm/min, and 650 rpm to 132 mm/min. The welding thermal history behavior of the set of experiments shown in Fig. 10(b) is similar to the previous conditions shown in Fig. 10(a). On the other hand, Fig. 11(c) shows the temperature distribution in the welded joints with parameters of 800 rpm to 120 mm/min, 863 rpm to 90 mm/min, and 800 rpm to 60 mm/min, which experienced different thermal histories. In the latter set of experiments, the maximum temperature recorded was of 1278 °C in the specific set of parameters of 800 rpm and 120 mm/min, obtaining maximum temperatures with higher rotary speeds.

A comparison of selected set of parameters between experimental and prediction data of the FSSW of Ti6Al4V plates is shown in Table 4. It was observed that the numerical values showed good approximation with the experimental data. The maximum registered temperature in experiments was 1278 and 1380 °C in the numerical calculations, both for the joint processed with 800 rpm and 120 mm/min. Higher temperatures in the numerical model could be associated with the flow model parameters and thermal properties of the tool.

The results obtained from the micro-hardness tests of the specimens joined with the different parameters are shown in Fig. 12. The hardness decrease at the HAZ is attributed to a coarser grain size resulting from the thermal gradients during friction welding. The hardness values of the SZ and TMAZ, which exhibit highly deformed grains, differ only slightly (by ~ 5 HV).

The pattern in Fig. 12(a) shows the variation of the hardness experienced by the FSSW joints. The values were obtained starting from the SZ, TMAZ, HAZ, and MB. The highest hardness value measured at the SZ was obtained from the experiment processed with 500 rpm and 120 mm/min, with a value of 373.3 HV. On the other hand, the lowest hardness values at the TMAZ and HAZ were 303.2 and 280.2 HV, respectively, which were observed in the experiment processed at 438 rpm with 90 mm/min, while the hardness value for the
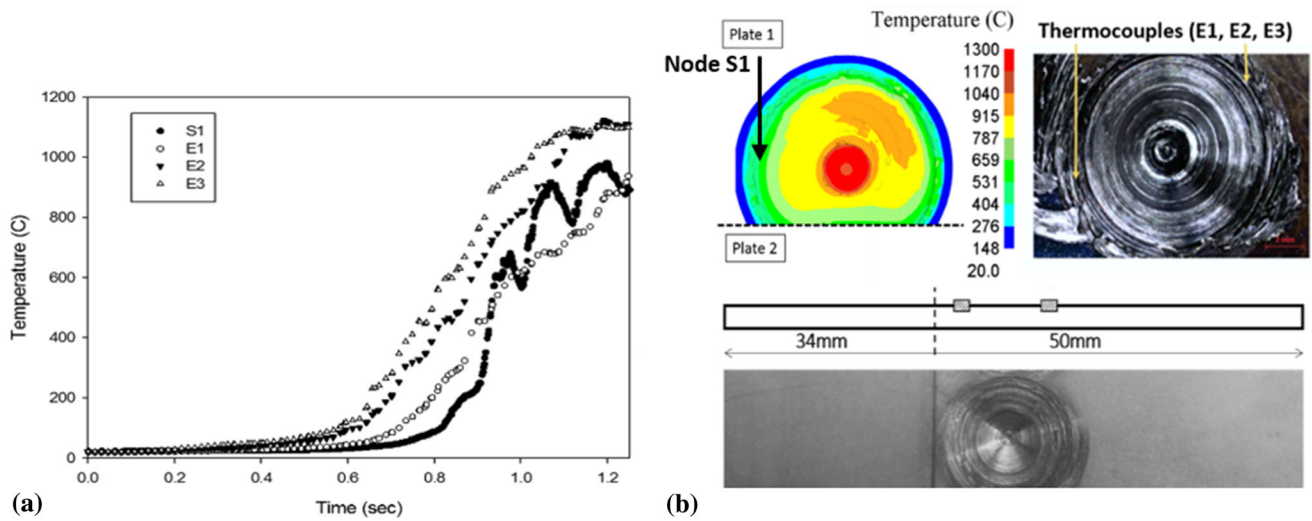
Fig. 10 Experimental and numerical results during the FSSW at 500 rpm and 120 mm/min: (a) plot of temperature evolution and (b) welding spot
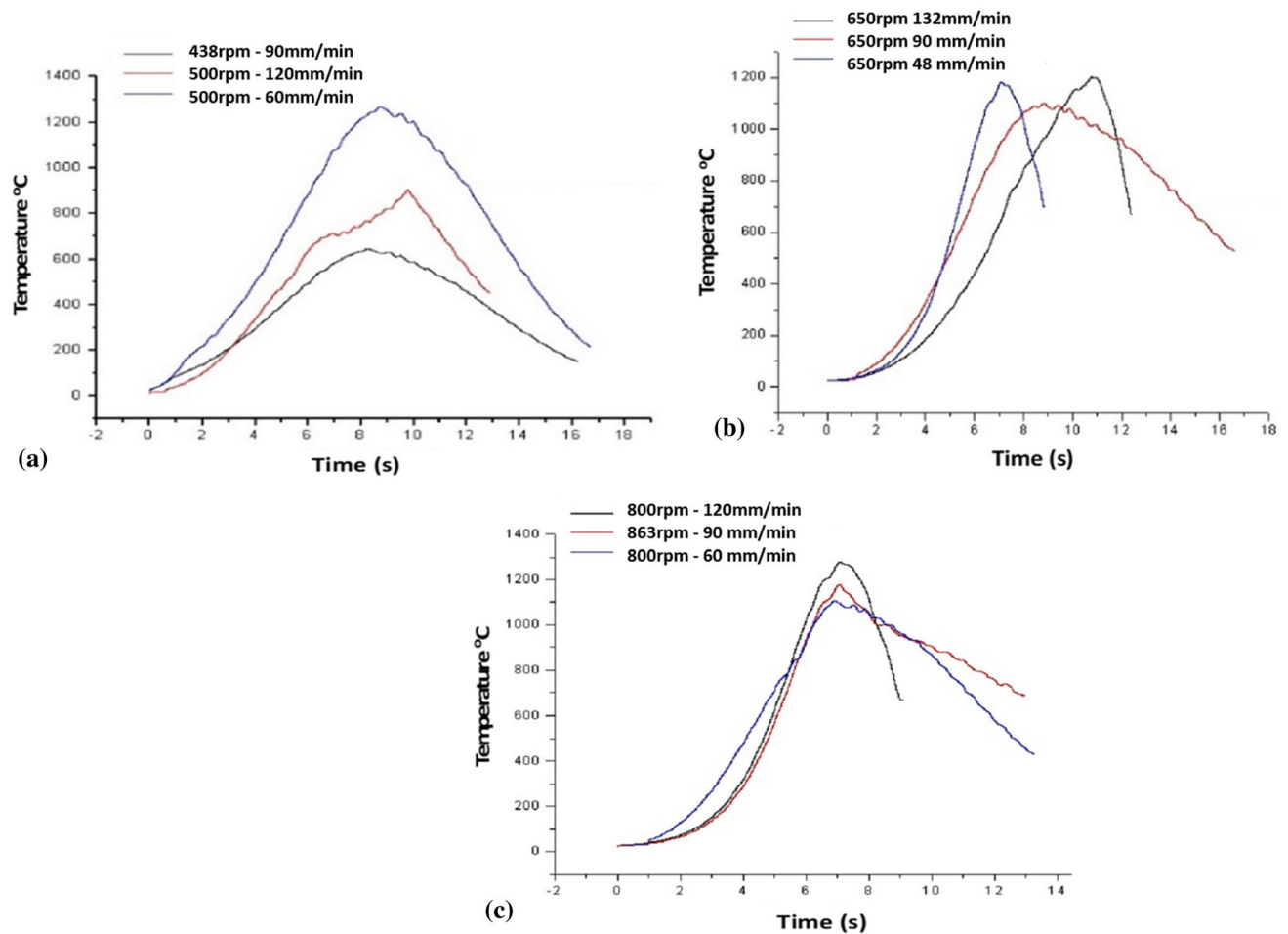

Fig. 11 Experimental temperature of the welded joints: (a) 438 and 500 rpm; (b) 650 rpm and (c) 800 and 863 rpm with different feed rate values

BM was 363.2 HV on average. A similar trend is observed for 650 rpm to 90 mm/min, if we compared with 500 rpm to 90 mm/min in Fig. 12(a). However, higher penetration speeds, as shown in Fig. 12(a), (b), and (c), show a decrease in average hardness for the HAZ region; the decrease in hardness in the HAZ can be explained by the annealing effect caused by the heating generated by friction. Figure 12(b) illustrates the micro-hardness profile of the samples processed with a rotational

Table 4 Experimental and numerical results of the maximum temperature

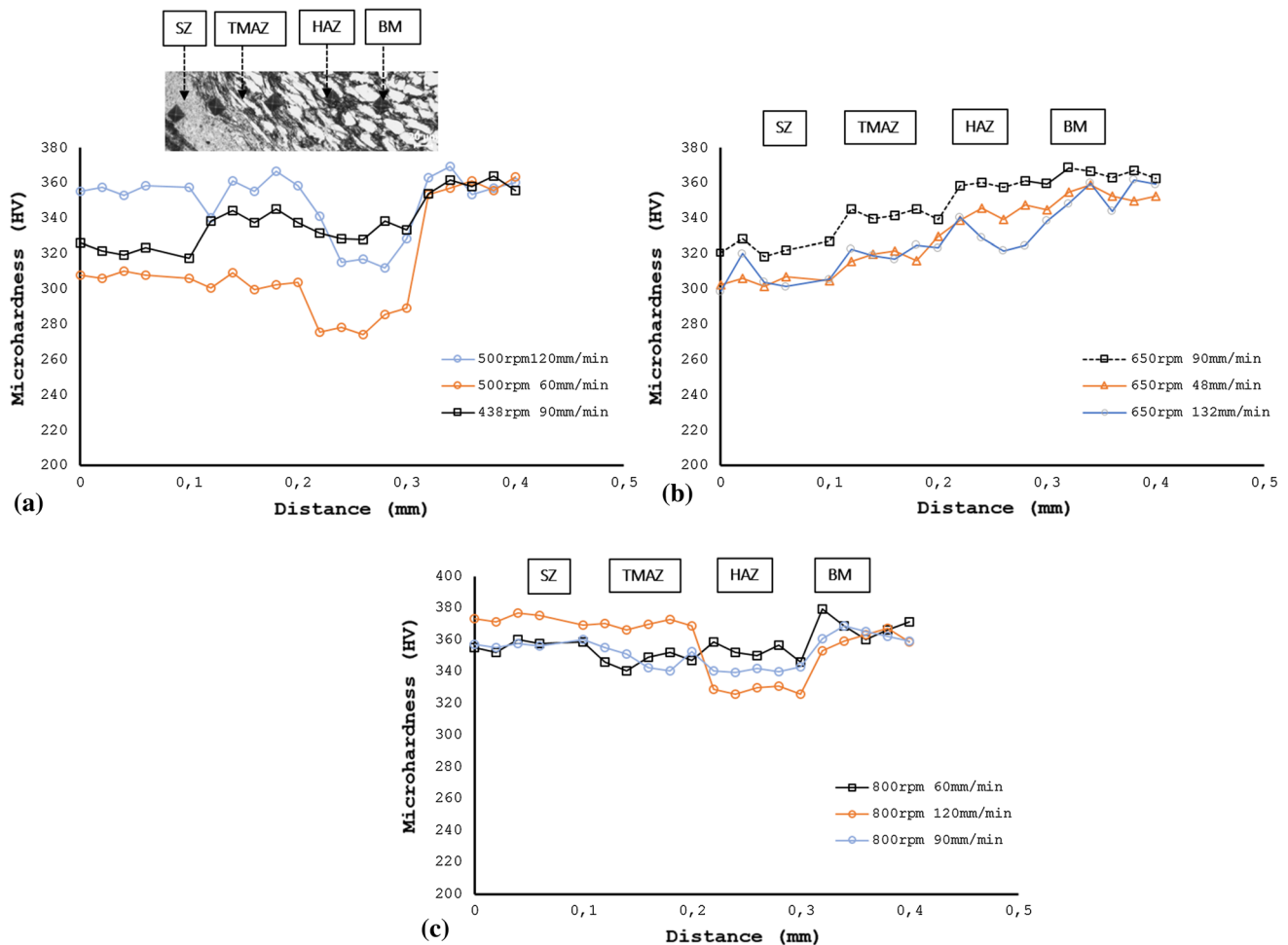| Test, rpm, mm/min	Experimental, °C	Simulated, °C	Difference, %
650, 90	1179	1230	4.3
650, 48	1220	1020	16.4
800, 120	1278	1380	7.9
500, 120	904	1210	33.7
438, 90	638	726	13.6
650, 132	1250	1360	8.7
800, 60	1105	1200	8.6
500, 60	1268	1380	8.8
863, 90	1198	1290	7.6

Fig. 12 Micro-hardness of samples at different process parameters: (a) 500 rpm with 120 and 60 mm/min and 438 rpm with 90 mm/min; (b) 650 rpm with 90, 48, and 132 mm/min; and (c) 800 rpm with 60 mm/min, 800 rpm with 120 mm/min, and 863 rpm with 90 mm/min

velocity of 650 rpm and 90, 48, and 132 mm/min, where the hardness value of the SZ presents the lower value (298 HV) during the test of 650 rpm and 132 mm/min. At higher values of feed rate, heat generation decreases, influencing the hardness values of the samples. Figure 12(c) describes the micro-hardness behavior of the experiments with rotation speed of 800 rpm to 120 and 60 mm/min and 863 rpm to 90 mm/min. The lowest hardness value measured in the SZ was at the experiment processed with 800 rpm and 90 mm/min, resulting in a value of 350 HV. It was observed that the HAZ presented a lower hardness value than that of the base metal; the annealing

produced by the friction process at the HAZ induced the hardness reduction in this zone. The welded joints presented a nugget pull-out failure, or also known as a failure by detachment, in one of the zones present at the union by means of FSSW.

The joints presented a circumferential nugget failure type in the HAZ. This area exhibited the lowest hardness measurement among the three zones compared with the BM, becoming the failure zone during the tension testing of the welds. The shear testing results of Fig. 13 show a tendency of increasing resistance with increasing rotational velocity. Specifically, at a

speed of 800 rpm, a feed rate of 120 mm/min, and a 3-s reside time, it was observed that the resistance for the joint reached a maximum of 40 kN. A lower value of 15 kN was observed at 650 rpm with a feed rate of 90 mm/min. Figure 14 shows fracture images of conditions at 800 rpm to 120 mm/min presenting a nugget pull-out failure mode. The joints fractured in the stir zone after shearing, and failure occurred at the bottom sheet. The zone with the lowest bonding strength is situated at the joining interface where both mixing and voids exist. Previous studies have demonstrated that in FSW having a heterogeneous hardness distribution fails in the lower hardness region, and the tensile properties of the joint are dependent on this re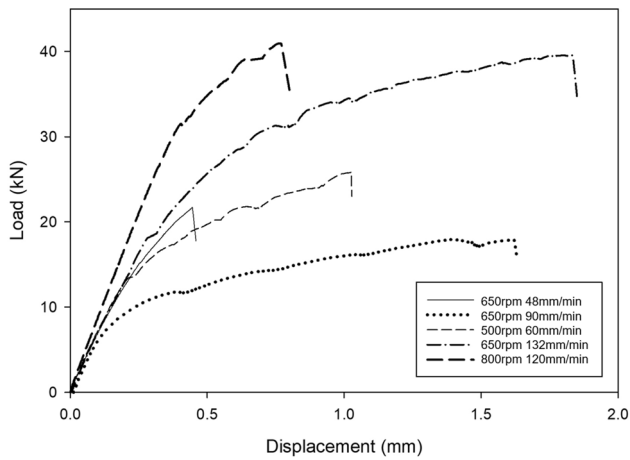gion of the joint. The failure of specimens at the HAZ is due to the recrystallization phenomena, which is characterized by a grain refinement. Fine grains cannot maintain dislocations; thus, the hardness deviates from Hall–Petch relationship (Ref 37). The strength of Ti alloys is influenced by the grain size and morphology, as well as by the quantity of α and β phases.

In the developed numerical model at 500 rpm and 120 mm/min, the highest value of effective strain corresponds to the center of the weld with a value of 8; this value decreases until reaching approximately a value of 5 at the limit of the nugget, see Fig. 15(a). The effective strain exhibits a substantial increase at the center of the weld. In all cases, it is observed that the maximum effective strain occurs in the contact area between the shoulder of the tool and the sheets to be joined. This can be attributed to the fact that there is more contact area between the shoulder of the tool than the contact of the pin. The effective strain results oscillate between 8 and 11 for the conditions evaluated. Buffa et al. (Ref 29) report that a strain value of approximately 10 and temperatures in the range of 890-920 °C will transform the initial structure of Ti6Al4V to the bimodal α + β structure during the FSW process, whereas temperatures less than 850 °C will result in evolution of the α phase. This combined effect of temperature and strain is the main cause of the microstructure transformation during the welding process. Meanwhile, Fig. 15(b) shows how the effective stress fluctuates at the nugget zone reaching a maximum at the center of the welding spot. The material flow plays a fundamental role in the friction welding process, as it determines the effectiveness of the joint. The flow of material around the tool is very complex, and the results depend on the correct selection of the geometry of the tool and the operating parameters considering the properties of the material to be joined.
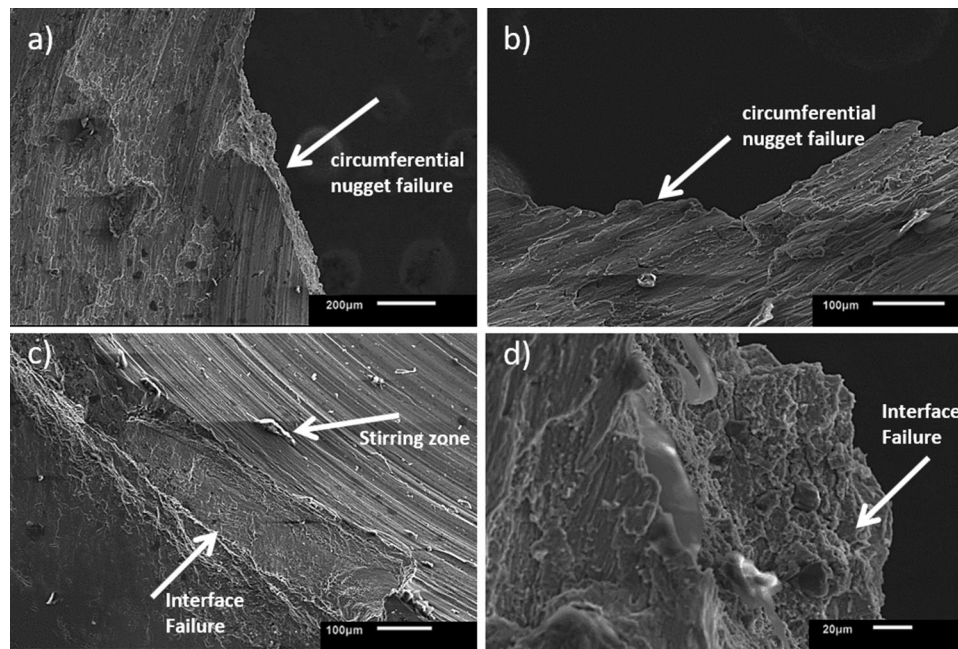

Fig. 13 (a) Shear strength of conditions at 650 rpm (48, 90, and 132 mm/min), 500 rpm to 60 mm/min, and 800 rpm to 120 mm/min

Fig. 14 SEM fracture images of conditions at 800 rpm to 120 mm/min presenting a nugget pull-out failure mode
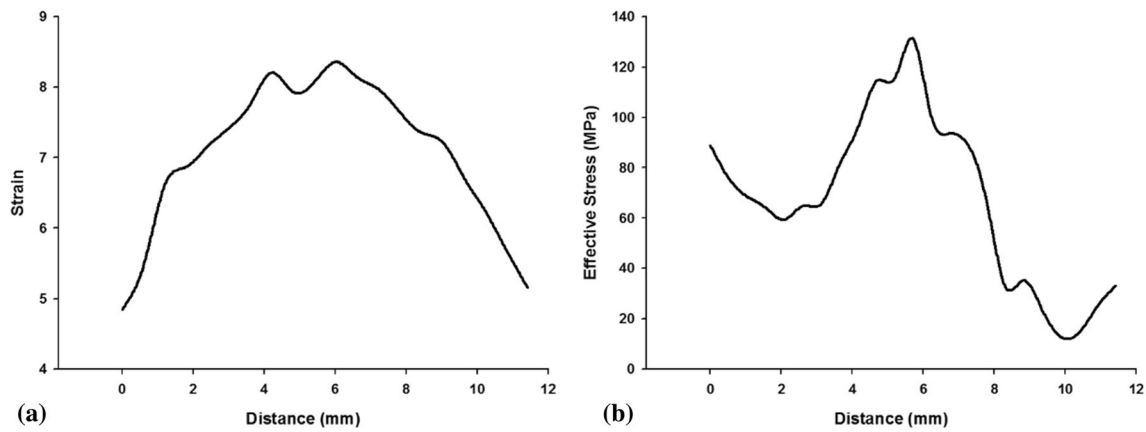
Fig. 15 Numerical results during FSSW process at 500 rpm to 120 mm/min: (a) strain vs. nugget zone distance and (b) stress vs. distance

5. Conclusions

The process variables such as rotational speed, axial feed rate, and reside time were evaluated, both experimentally and by means of numerical models, in order to predict thermal and mechanical effects in FSSW. The following inferences are derived from the current work:

- The welding microstructures show different effects due to the temperature gradient. The maximum welding temperature recorded was greater than the β-transus temperature. The welding microstructure in the SZ was transformed into a α + β microstructure. The maximum temperature and feed rate notably affected the properties of the joint, whereas the grain size evolution was affected principally by the temperature of the welding joint. Rotational speed and feed rate are the principal variables that affect the temperature during the FSSW process. High axial feed rates tend to reduce the heat input and temperature.
- The experiments showed that a high rotary speed increased the process temperature in Ti6Al4V due to the low thermal conductivity of the material. The experimental temperature reached a maximum value of 1279 °C for a rotational speed and feed rate of 800 rpm and 120 mm/min; a highest temperature of 1105 °C was recorded for the same rotational velocity and a feed rate of 60 mm/min. In the case of a rotational speed of 500 rpm and feed rates of 60 and 120 mm/min, a maximum temperature of 1268 °C and a minimum value of 904 °C were obtained. It was observed that, at lower axial feed rate of penetration, the temperature was higher than at 120 mm/min, which was attributed to insufficient contact time in order to produce enough heat to elevate the temperature during the process. The HAZ and BM in the joint formed at 500 rpm and 60 mm/min showed a higher hardness value of 373 HV. The lowest value of 342 HV corresponded to 800 rpm and 120 mm/min. At higher axial feed rates, a decrease in heat generation is observed. In general, the HAZ exhibited a lower hardness compared to the BM, which was attributed to the annealing effect caused by friction heating.
- The tension tests showed rupture at the HAZ; this behavior was attributed to a recrystallized zone characterized by fine grains. The strength of Ti alloys is influenced by the grains size and morphology, as well as the quantity of α and β phases.
- The distinctive characteristic of the numerical model is the flow of a convex welding tool to weld Ti6Al4V lap joints. The numerical model predicts a non-symmetric effective stress and effective strain of the FSSW of Ti6Al4V. The temperature profile is nearly symmetric in the weld section, which is caused by the material movement from the top plate toward the tool center; a half-sphere shape is formed below the center of the shoulder tool. The agreement between the predicted and recorded temperatures was considered to be adequate in relation to the highest temperature and slopes of the curves.

References

1. C. Cui, B.M. Hu, L. Zhao, and S. Liu, Titanium Alloy Production Technology, Market Prospects and Industry Development, *Mater. Des.*, 2011, https://doi.org/10.1016/j.matdes.2010.09.011
2. X. Zhan, Y. Liu, J. Liu, Y. Meng, Y. Wei, J. Yang, and X. Liu, Comparative Study on Experimental and Numerical Investigations of Laser Beam and Electron Beam Welded Joints for Ti6Al4V Alloy, *J. Laser Appl.*, 2017, https://doi.org/10.2351/1.4975824
3. C. Qi, X. Zhan, Q. Gao, L. Liu, Y. Song, and Y. Li, The Influence of the Pre-placed Powder Layers on the Morphology, Microscopic Characteristics and Microhardness of Ti-6Al-4V/WC MMC Coatings during Laser Cladding, *Opt. Laser Technol.*, 2019, https://doi.org/10.1016/j.optlastec.2019.105572
4. X. Zhan, H. Bu, Q. Gao, T. Yan, and W. Ling, Temperature Field Simulation and Grain Morphology on Laser Welding-Brazing Between Ti-6Al-4V and 1050 Aluminum Alloy, *Mater. Res. Express.*, 2019, https://doi.org/10.1088/2053-1591/ab061a
5. P. Chai, W. Hu, S. Ji, X. Ai, Z. Lv, and Q. Song, Refill Friction Stir Spot Welding Dissimilar Al/Mg Alloys, *J. Mater. Eng. Perform.*, 2019, **28**, p 6174–6181. https://doi.org/10.1007/s11665-019-04359-7
6. D. Trimble, G.E. O'Donnell, and J. Monaghan, Characterisation of Tool Shape and Rotational Speed for Increased Speed during Friction Stir Welding of AA2024-T3, *J. Manuf. Process.*, 2015, https://doi.org/10.1016/j.jmapro.2014.08.007

7. A. Toumpis, A. Galloway, S. Cater, and N. McPherson, Development of a Process Envelope for Friction Stir Welding of DH36 Steel—A Step Change, *Mater. Des.*, 2014, https://doi.org/10.1016/j.matdes.2014.04.066

8. Y. Zhang, Y.S. Sato, H. Kokawa, S.H.C. Park, and S. Hirano, Microstructural Characteristics and Mechanical Properties of Ti-6Al-4V Friction Stir Welds, *Mater. Sci. Eng., A*, 2008, https://doi.org/10.1016/j.msea.2007.08.051

9. H. Papahn, P. Bahemmat, M. Haghpanahi, and I.P. Aminaie, Effect of Friction Stir Welding Tool on Temperature, Applied Forces and Weld Quality, *IET Sci. Meas. Technol.*, 2015, https://doi.org/10.1049/iet-smt.2014.0150

10. H. Fujii, Y. Sun, H. Kato, and K. Nakata, Investigation of Welding Parameter Dependent Microstructure and Mechanical Properties in Friction Stir Welded Pure Ti Joints, *Mater. Sci. Eng., A*, 2010, https://doi.org/10.1016/j.msea.2010.02.023

11. S. Mironov, Y. Zhang, Y.S. Sato, and H. Kokawa, Development of Grain Structure in β-Phase Field during Friction Stir Welding of Ti-6Al-4V Alloy, *Scr. Mater.*, 2008, https://doi.org/10.1016/j.scriptamat.2008.02.014

12. K. Kitamura, H. Fujii, Y. Iwata, Y.S. Sun, and Y. Morisada, Flexible Control of the Microstructure and Mechanical Properties of Friction Stir Welded Ti-6Al-4V Joints, *Mater. Des.*, 2013, https://doi.org/10.1016/j.matdes.2012.10.051

13. W.S. Lee and C.F. Lin, High-Temperature Deformation Behaviour of Ti6A14V Alloy Evaluated by High Strain-Rate Compression Tests, *J. Mater. Process. Technol.*, 1998, https://doi.org/10.1016/S0924-0136(97)00302-6

14. H.J. Liu, L. Zhou, and Q.W. Liu, Microstructural Characteristics and Mechanical Properties of Friction Stir Welded Joints of Ti-6Al-4V Titanium Alloy, *Mater. Des.*, 2010, https://doi.org/10.1016/j.matdes.2009.08.025

15. L. Zhou, H.J. Liu, and Q.W. Liu, Effect of Rotation Speed on Microstructure and Mechanical Properties of Ti-6Al-4V Friction Stir Welded Joints, *Mater. Des.*, 2010, https://doi.org/10.1016/j.matdes.2009.12.014

16. J. Wang, J. Su, R.S. Mishra, R. Xu, and J.A. Baumann, Tool Wear Mechanisms in Friction Stir Welding of Ti-6Al-4V Alloy, *Wear*, 2014, https://doi.org/10.1016/j.wear.2014.09.010

17. S. Yoon, R. Ueji, and H. Fujii, Effect of Rotation Rate on Microstructure and Texture Evolution during Friction Stir Welding of Ti-6Al-4V Plates, *Mater. Charact.*, 2015, https://doi.org/10.1016/j.matchar.2015.06.025

18. H. Jamshidi Aval, Microstructure and Residual Stress Distributions in Friction Stir Welding of Dissimilar Aluminium Alloys, *Mater. Des.*, 2015, https://doi.org/10.1016/j.matdes.2015.08.050

19. X.W. Yang, T. Fu, and W.Y. Li, Friction Stir Spot Welding: A Review on Joint Macro- and Microstructure, Property, and Process Modelling, *Adv. Mater. Sci. Eng.*, 2014, https://doi.org/10.1155/2014/697170

20. X. Song, L. Ke, L. Xing, F. Liu, and C. Huang, Effect of Plunge Speeds on Hook Geometries and Mechanical Properties in Friction Stir Spot Welding of A6061-T6 Sheets, *Int. J. Adv. Manuf. Technol.*, 2014, https://doi.org/10.1007/s00170-014-5632-y

21. Y. Bozkurt, S. Salman, and G. Çam, Effect of Welding Parameters on Lap Shear Tensile Properties of Dissimilar Friction Stir Spot Welded aa 5754-h22/2024-t3 Joints, *Sci. Technol. Weld. Join.*, 2013, https://doi.org/10.1179/1362171813Y.0000000111

22. F.A. Garcia-Castillo, F.J. García-Vázquez, F.A. Reyes-Valdés, P.C. Zambrano-Robledo, G.M. Hernández-Muñoz, and E.R. Rodríguez-Ramos, Microstructural Evolution in Ti-6Al-4V Alloy Joints Using the Process of Friction Stir Spot Welding, *Weld. Int.*, 2018, **32**, p 570–578. https://doi.org/10.1080/09507116.2017.1347346

23. D. Kim, H. Badarinarayan, I. Ryu, J.H. Kim, C. Kim, K. Okamoto, R.H. Wagoner, and K. Chung, Numerical Simulation of Friction Stir Spot Welding Process for Aluminum Alloys, *Met. Mater. Int.*, 2010, https://doi.org/10.1007/s12540-010-0425-9

24. P. Fanelli, F. Vivio, and V. Vullo, Experimental and Numerical Characterization of Friction Stir Spot Welded Joints, *Eng. Fract. Mech.*, 2012, https://doi.org/10.1016/j.engfracmech.2011.07.009

25. S. Mandal, J. Rice, and A.A. Elmustafa, Experimental and Numerical Investigation of the Plunge Stage in Friction Stir Welding, *J. Mater. Process. Technol.*, 2008, **203**, p 411–419. https://doi.org/10.1016/j.jmatprotec.2007.10.067

26. M. Awang, V.H. Mucino, Z. Feng, S.A. David, Thermo-mechanical Modeling of Friction Stir Spot Welding (FSSW) Process: Use of an Explicit Adaptive Meshing Scheme, in: SAE Tech. Pap. (2005). https://doi.org/10.4271/2005-01-1251

27. G. D'Urso and C. Giardini, FEM Model for the Thermo-mechanical Characterization of Friction Stir Spot Welded Joints, *Int. J. Mater. Form.*, 2016, https://doi.org/10.1007/s12289-015-1218-y

28. Z. Zhang and H.W. Zhang, Numerical Studies on Controlling of Process Parameters in Friction Stir Welding, *J. Mater. Process. Technol.*, 2009, https://doi.org/10.1016/j.jmatprotec.2008.01.044

29. G. Buffa, L. Fratini, M. Schneider, and M. Merklein, Micro and Macro Mechanical Characterization of Friction Stir Welded Ti-6Al-4V Lap Joints through Experiments and Numerical Simulation, *J. Mater. Process. Technol.*, 2013, https://doi.org/10.1016/j.jmatprotec.2013.07.003

30. J.J. Swab, L. Vargas-Gonzalez, E. Wilson, and E. Warner, Properties and Performance of Polycrystalline Cubic Boron Nitride, *Int. J. Appl. Ceram. Technol.*, 2015, **12**, p E74–E81. https://doi.org/10.1111/ijac.12380

31. A.L. Pilchak and J.C. Williams, Microstructure and Texture Evolution during Friction Stir Processing of Fully Lamellar Ti-6Al-4V, *Metall. Mater. Trans. A Phys. Metall. Mater. Sci.*, 2011, https://doi.org/10.1007/s11661-010-0434-9

32. K.H. Muci-Küchler, S. Kalagara, and W.J. Arbegast, Simulation of a Refill Friction Stir Spot Welding Process Using a Fully Coupled Thermo-mechanical FEM Model, *J. Manuf. Sci. Eng. Trans. ASME*, 2010, https://doi.org/10.1115/1.4000881

33. Z. Xu, Z. Li, Z. Lv, and L. Zhang, Effect of Tool Rotating Speed on Microstructure and Mechanical Properties of Friction Stir Lap Welded Ti–6Al–4V Alloy, *Int. J. Adv. Manuf. Technol.*, 2017, **90**, p 3793–3800. https://doi.org/10.1007/s00170-016-9741-7

34. S. Mironov, Y. Zhang, Y.S. Sato, and H. Kokawa, Crystallography of Transformed β Microstructure in Friction Stir Welded Ti-6Al-4V Alloy, *Scr. Mater.*, 2008, https://doi.org/10.1016/j.scriptamat.2008.04.038

35. J.W. Elmer, T.A. Palmer, S.S. Babu, W. Zhang, and T. DebRoy, Phase Transformation Dynamics during Welding of Ti-6Al-4V, *J. Appl. Phys.*, 2004, https://doi.org/10.1063/1.1737476

36. A.J. Ramirez and M.C. Juhas, Microstructural Evolution in Ti-6Al-4V Friction Stir Welds, *Mater. Sci. Forum*, 2003, https://doi.org/10.4028/www.scientific.net/msf.426-432.2999

37. T.G. Nieh and J. Wadsworth, Hall–Petch Relation in Nanocrystalline Solids, *Scr. Metall. Mater.*, 1991, https://doi.org/10.1016/0956-716X(91)90256-Z